Two-Dimensional Substitution Series $Na_3P_{1-x}Sb_xS_{4-y}Se_y$ Beyond Static Description of Structural Bottlenecks for Na^+ Transport

Till, Paul; Agne, Matthias T.; Kraft, Marvin A.; Courty, Matthieu; Famprikis, Theodosios; Ghidiu, Michael; Krauskopf, Thorben; Masquelier, Christian; Zeier, Wolfgang G.

DOI
10.1021/acs.chemmater.1c04445

Publication date
2022

Document Version
Final published version

Published in
Chemistry of Materials

CHEMISTRY OF MATERIALS

pubs.acs.org/cm

Article

Two-Dimensional Substitution Series $Na_3P_{1-x}Sb_xS_{4-y}Se_y$: Beyond Static Description of Structural Bottlenecks for Na^+ Transport

Paul Till, Matthias T. Agne, Marvin A. Kraft, Matthieu Courty, Theodosios Famprikis, Michael Ghidiu, Thorben Krauskopf, Christian Masquelier, and Wolfgang G. Zeier*

Cite This: *Chem. Mater.* 2022, 34, 2410−2421

Read Online

ACCESS | Metrics & More | Article Recommendations | Supporting Information

ABSTRACT: Highly conductive solid electrolytes are fundamental for all solid-state batteries with low inner cell resistance. Such fast solid electrolytes are often found by systematic substitution experiments in which one atom is exchanged for another, and corresponding changes in ionic transport are monitored. With this strategy, compositions with the most promising transport properties can be identified fast and reliably. However, the substitution of one element does not only influence the crystal structure and diffusion channel size (static) but also the underlying bonding interactions and with it the vibrational properties of the lattice (dynamic). Since both static and dynamic properties influence the diffusion process, simple one-dimensional substitution series only provide limited insights to the importance of changes in the structure and lattice dynamics for the transport properties. To overcome these limitations, we make use of a two-dimensional substitution approach, investigating and comparing the four single-substitution series $Na_3P_{1-x}Sb_xS_4$, $Na_3P_{1-x}Sb_xSe_4$, $Na_3PS_{4-y}Se_y$, and $Na_3SbS_{4-y}Se_y$. Specifically, we find that the diffusion channel size represented by the distance between S/Se ions cannot explain the observed changes of activation barriers throughout the whole substitution system. Melting temperatures and the herein newly defined anharmonic bulk modulus—as descriptors for bonding interactions and corresponding lattice dynamics—correlate well with the activation barriers, highlighting the relevance of lattice softness for the ion transport in this class of fast ion conductors.

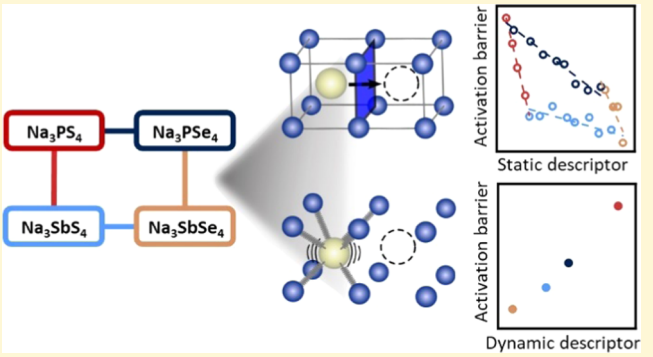

1. INTRODUCTION

All-solid-state batteries are investigated as a next-generation energy storage technology, replacing the nowadays used secondary cells that employ a liquid electrolyte. The replacement of the liquid with a solid electrolyte is predicted to enable the implementation of metal anodes, boosting the energy density and improving operation safety by removing the flammable electrolyte.[1,2] To lower the inner cell resistance, solid electrolytes with a high ionic conductivity are necessary. This need for highly conductive electrolytes has led to the discovery of Li^+ and Na^+ solid electrolytes with ionic conductivities, which surpass those of commonly used liquid electrolytes at and below room temperature.[3−6] In addition to the strive for high ionic conductivities, to enable technological advancements, much basic research has targeted a deeper understanding of ionic conduction processes of such Li^+- and Na^+-based materials. The macroscopic activation barrier is defined by the Arrhenius-like temperature dependence of the ionic conductivity, and for many fast ion conducting materials, it is used as an approximate for the migration enthalpy, i.e., the energetic needs for the ionic jump from one lattice site to an adjacent vacant one.[7] Consequently, the macroscopic activation barrier is a frequently used metric to study transport properties of solid ion conductors.[8−10]

Various guidelines for the impact of the crystal structure on the macroscopic activation barrier and with it the ionic transport have been derived.[7,9,11] Fundamentally, a good connectivity has to exist between the coordination polyhedra of the mobile ion.[7,12] The connection between these coordination polyhedra further determines the activation barrier height. Edge-sharing polyhedra are less favorable for ion transport than face sharing polyhedra since the diffusion bottleneck is generally smaller in the former, and the coordination environment of the mobile ion undergoes more changes during the jump process.[7,12] The diffusion bottleneck of one polyhedra connection type can be tailored by substituting larger atoms into the structure, which generally results in a decrease in the activation barrier (compare Figure

Received: December 29, 2021
Revised: February 10, 2022
Published: February 25, 2022

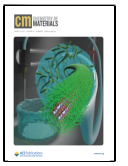

1), due to a widening of the diffusion bottleneck.[9,13,14] These effects can be summarized under the term of static influences.

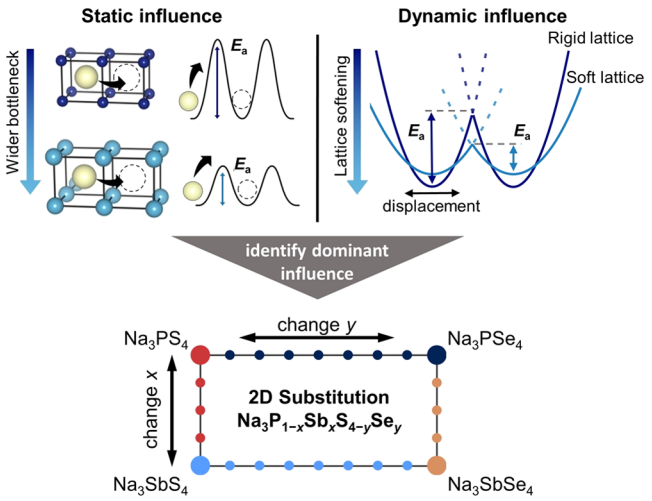

Figure 1. Schematic representations for static and dynamic influences on the activation barrier E_a. Static influence: For a successful ion jump, the host lattice needs to distort and generate space for the mobile ion to jump through. This distortion comes at an energetic cost. When the diffusion bottleneck is wider, less distortion is necessary, and hence, lower activation barriers are found. Dynamic influence: considering a strain-energy derived model, the activation barrier can be lowered by lattice softening. In a rigid lattice, the mobile ion is held close to its equilibrium position. In a soft lattice, the mobile ion vibrates in a flatter potential well and can be displaced further away from its equilibrium position. In substitution series, both effects are present. The 2D substitution series are a helpful way to investigate if one of the effects is dominating over the other. A schematic of such a 2D substitution series, presented in this work, is shown at the bottom. Small dots correspond to intermediate compositions of the substitution series.

Besides static effects, the vibrational characteristics of the crystal lattice, i.e., dynamic influences, have also been suggested to impact the transport properties.[11,15] These influences have been studied for decades[16−18] and have recently drawn increased research focus in materials relevant for solid-state batteries.[15,19−21] In a simple strain-energy derived relation, an ionic jump happens as soon as the mobile ion is displaced from a stable lattice site beyond a specific threshold and the activation energy should then correspond to the strain energy for this displacement, as shown in Figure 1.[22] Therefore, by altering the bonding interactions and with it the potential wells around the migrating ion, the activation barrier can be tuned.[7,8] This is usually achieved by substitutions of the immobile ion framework. Following the paradigm of "the softer, the better", the introduction of ions with higher polarizability leads to a weakening of bonding interactions, softer lattice vibrations, and consequently flatter energy landscapes, which ultimately result in lower activation barriers. Indeed, for many sulfide-based materials, lower activation barriers than those of the harder oxides can be found,[8,23,24] and overall, the strength of the bonding interaction between the mobile ion and its framework seems to be paramount.[10,25]

Static and dynamic influences on the activation barrier have been commonly investigated in substitution series forming full solid solutions, where correlations between changing the crystal structure or lattice softness and the altered activation barrier have been found for various material systems.[26,27] By nature however, isovalent substitution leads to simultaneous changes of the crystal structure and lattice dynamics, and in turn, a simultaneous change of static and dynamic influences occurs. This inevitable convolution and concurrent change of both quantities makes it nearly impossible to decide to which extent the observed activation barrier changes are caused by a static or dynamic effect. In addition, other fundamental factors may be completely overshadowed by incomplete descriptors for the observed activation barrier changes, potentially resulting in misleading and ineffective design guidelines.

To overcome the shortcomings of single-substitution series, a "two-dimensional" (2D) substitution approach as schematically shown in Figure 1 is used to combine investigations of four substitution series within one structure family, which makes it possible to identify descriptors that can explain activation barrier changes for one structure family and are not only valid for one single-substitution series. This was demonstrated in the case of the $Li_4Ge_{1-x}Sn_xS_{4-y}Se_y$ system, where the comparison of four substitution series leads to a deeper understanding of structural changes with composition, and the existence of an optimal Li^+ coordination polyhedral volume for ionic conductivity was found.[28]

In this study, we investigated the $Na_3P_{1-x}Sb_xS_{4-y}Se_y$ system to gain a better understanding of how dynamic and static changes influence the activation barrier and if one factor is dominating in this class of materials. Materials with the Na_3PnCh_4 (*Pn* = P, Sb; *Ch* = S, Se) structure have been continuously investigated for possible application in batteries,[29−31] and very recently, record high ionic conductivities of up to 40 mS/cm were reported for W-doped Na_3SbS_4.[6,32] Even more important, the Na_3PnCh_4 system is a perfect candidate for a 2D substitution approach since the building blocks of the structure—the immobile polyanionic backbone—as well as the distribution of Na^+ positions barely change throughout the investigated material system.[20,30,31,33] In other words, no major changes of the transport mechanism (near room temperature) are expected, and therefore, the observed changes in the activation barrier can be assigned to changes of static and dynamic influences. In this work, the investigation of structural changes was carried out by X-ray diffraction and subsequent Rietveld refinements. The dynamical properties were characterized by means of melting temperatures and the herein newly defined anharmonic weighted bulk modulus, which can be obtained from temperature-dependent X-ray diffraction. While the static descriptors were found to be insufficient to explain activation barrier changes, the altered dynamic properties were identified as the main driving force. Overall, the approach of "two-dimensional substitutions" is a stepping stone for better understanding the convoluted influences on ionic transport in superionic conductors.

2. EXPERIMENTAL SECTION

2.1. Experimental Details for the Substitution Series $Na_3PS_{4-y}Se_y$. All crystallographic data and transport information of the substitution series $Na_3PS_{4-y}Se_y$ were taken from ref 20. All information for sample preparation, X-ray diffraction, and impedance measurement details can be found there. Experimental details for the three remaining substitution series $Na_3P_{1-x}Sb_xS_4$, $Na_3P_{1-x}Sb_xSe_4$, and $Na_3SbS_{4-y}Se_y$ are described below.

2.2. Synthesis. All sample preparations were carried out in an Ar-filled glove box (MBraun). For the reaction, samples were placed in quartz ampoules that were dried under dynamic vacuum at 800 °C for

https://doi.org/10.1021/acs.chemmater.1c04445
Chem. Mater. 2022, 34, 2410−2421

2 h to remove all traces of water. The precursor materials Na_2Se and Sb_2Se_3 were synthesized beforehand for further use. Na_2Se was prepared via a gas phase reaction as reported elsewhere using elemental Na and Se.[20] For the Sb_2S_3 synthesis, elemental Sb (99.999% trace metals basis, ChemPur) and S (99.999% trace metals basis, Acros Organics) were mixed in an agate mortar for 10 min, pelletized, and sealed in an ampoule under vacuum. For the reaction, the following temperature profile was applied. Heating to 650 °C (rate of 100 °C/h) dwelled for 20 min, then cooled down to 520 °C (rate of 20 °C/h), and held for 24 h.[6] The obtained product was ground into a powder for further use.

The substitution series $Na_3P_{1-x}Sb_xS_4$, $Na_3P_{1-x}Sb_xSe_4$, and $Na_3SbS_{4-y}Se_y$ were prepared by solid-state ampoule synthesis. As far as possible, binary salts were used for the synthesis. Elemental precursors were used in the case of unavailability of the binaries or to balance reaction equations. For $Na_3P_{1-x}Sb_xS_4$, the precursors were Na_2S (Sigma-Aldrich), P_2S_5 (99%, Sigma-Aldrich), Sb (99.999% trace metals basis, ChemPur), and S (99.999% trace metals basis, Acros Organics). For $Na_3P_{1-x}Sb_xSe_4$, the precursors were Na_2Se, P (99.995% trace metals basis, ChemPur), Sb, and Se (99.5% trace metals basis, Alfa Aesar), and for $Na_3SbS_{4-y}Se_y$, the precursors Na_2S, Na_2Se, Sb_2S_3, Sb, S, and Se were used. The precursors were mixed in stoichiometric ratios and hand-ground in an agate mortar for 20 min. The obtained powders were pelletized, loaded into quartz ampoules (12 mm inner diameter), and sealed under vacuum. The reaction was carried out at 500 °C for 20 h (heating ramp of 30 °C/h). After the reaction, the ampoules were opened in a glove box, and the obtained pellets were ground into powders for further use.

2.3. Laboratory X-ray Diffraction. Powder X-ray diffraction patterns were recorded using a PANalytical Empyrean powder diffractometer in a Bragg–Brentano θ–θ geometry with Cu Kα radiation (λ_1 = 1.5405980 Å; λ_2 = 1.5444260 Å; $I(\lambda_2)/I(\lambda_1)$ = 0.5) and a PIXcel detector. A 2θ range of 10–90° with a step size of 0.026° and an irradiation time of 200 s per step was used. Powder samples were placed on a (911)-oriented silicon zero background disc and sealed with a Kapton polyimide film (7.5 μm) in an airtight sample holder for the measurement.

2.4. Synchrotron X-ray Diffraction. Synchrotron X-ray diffraction was measured at the I11 beamline at Diamond Light Source (Oxfordshire, UK). Powder samples of Na_3PS_4, Na_3SbS_4, Na_3PSe_4, and Na_3SbSe_4 were sealed in borosilicate capillaries under an argon atmosphere. The diameters of the capillaries were 0.5 mm for sulfide-based samples and 0.3 mm for the selenide-based samples. The capillaries were mounted on a sample spinner for the measurements, which were carried out in a 2θ range of 0–150° with a step size of 0.005° and a total irradiation time of 30 min per measurement. Monochromatic X-rays with a wavelength of 0.826497 Å were used. Diffraction patterns were recorded using multi-analyzing crystal (MAC) detectors at temperatures in the range from 100 to 300 K in 50 K steps using a Cryostream Plus to adjust the temperature.

2.5. Rietveld Refinements. Rietveld refinements were carried out using the TOPAS V6 Academic software package (Coelho Software, Brisbane, Australia).[34] For diffraction patterns collected on a laboratory diffractometer, data recorded for 2θ angles lower than 22° were excluded in the refinement due to the high background caused by the Kapton polyimide film.[20] The background was modeled with a Chebyshev polynomial function using 30 free coefficients. The reflection shape was described by a Thompson–Cox–Hastings pseudo-Voigt function, and reflection asymmetry was considered using a simple axial model. For the synchrotron diffraction patterns, refinements were carried out between 7 and 50° for Na_3PS_4, Na_3SbS_4, and Na_3SbSe_4 and between 7 and 47° for Na_3PSe_4. The background was described by manually placed and fixed background points. A Pearson-type VII function was used for the reflection shape description and a simple axial model for the reflection asymmetry. The parameters for all diffractograms were refined in the following order: (i) the scale factor, lattice parameters, and sample height displacements; (ii) the reflection profile; and (iii) the reflection asymmetry. Once a good profile fit was obtained, the structural parameters were refined: (iv) atomic coordinates, (v) isotropic thermal displacement parameters, (vi) and occupancies of the P, Sb, S, and Se ions, respectively. Eventually, all parameters were refined simultaneously to ensure the stability of the refined values.

2.6. Electrochemical Impedance Spectroscopy (EIS). AC impedance spectroscopy was used to determine electrical conductivities using an SP-300 impedance analyzer (Bio-Logic Science instruments Ltd.). Measurements of the three substitution series $Na_3P_{1-x}Sb_xS_4$, $Na_3P_{1-x}Sb_xSe_4$, and $Na_3SbS_{4-y}Se_y$ were performed in a temperature range of 253–333 K in steps of 10 K with an intermediate step at 297 K and 1 h equilibration time per temperature, utilizing a sinusoidal excitation voltage signal at frequencies of 7 MHz to 100 mHz with an amplitude of 10 mV. For the measurements, powder samples were pelletized and pressed isostatically at 400 MPa vessel pressure. Electrical contact to the pellets was ensured by thermally evaporated Au electrodes (200 nm thickness on each pellet side). The gold electrodes were contacted with aluminum current collectors, and the pellets were sealed in pouch bags.

2.7. Differential Scanning Calorimetry. Differential scanning calorimetry (DSC) was performed with a NETZSCH STA 449F3 housed in an Ar-filled glovebox (Jacomex). For the measurement, sample powder was loaded into quartz crucibles and Ar gas flow was adjusted to 40 mL/min. The temperature was increased from 313 to 1073 K and again cooled down to 313 K with 5 K per minute.

3. RESULTS

3.1. Structural Characterization. Three polymorphs have been observed in the Na_3PnCh_4 structure type (Pn = P, As, Sb; Ch = S, Se). The typical high-temperature cubic polymorph crystallizes in the space group $I\bar{4}3m$, in which the $PnCh_4^{3-}$ tetrahedra construct a body-centered cubic sublattice (shown in Figure 2a), and Na^+ occupies the octahedral voids (Wyckoff 6b position), forming a three-dimensionally interconnected Na^+ sublattice.

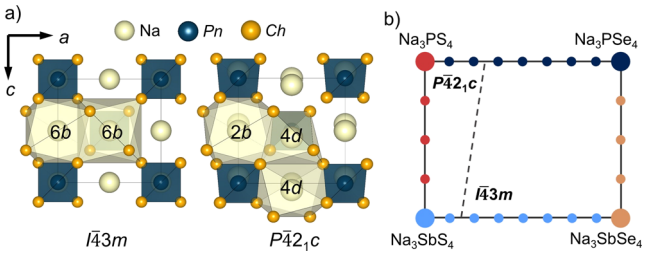

Figure 2. (a) Cubic (space group $I\bar{4}3m$) and tetragonal (space group $P\bar{4}2_1c$) polymorph of the Na_3PnCh_4 structure family. (b) 2D substitution scheme of the investigated Na_3PnCh_4 structure at room temperature. Each dot represents a composition, where the incremental change of the cations per dot is 0.25 and for the anions is 0.5. The transition from the tetragonal to the cubic polymorph is indicated by the dotted line. For clarity: At room temperature, the phase transition occurs between the compounds Na_3PS_3Se and $Na_3PS_{2.5}Se_{1.5}$ as well as between the compounds $Na_3SbS_{3.5}Se_{0.5}$ and Na_3SbS_3Se.

A tetragonal polymorph with space group $P\bar{4}2_1c$ is considered as the low-temperature stable modification of the Na_3PnCh_4 family (shown in Figure 2a). Group-subgroup relations suggest that the phase transition from cubic to tetragonal should occur via an intermediate phase (space group $I\bar{4}2m$),[35] which however has not been observed experimentally. Due to the phase transition, a tetragonal elongation of the c axis results in the splitting of the Na^+ positions, i.e., the Wyckoff position 6b splits into the special Wyckoff position 2a and the general Wyckoff position 4d. Furthermore, a slight

https://doi.org/10.1021/acs.chemmater.1c04445
Chem. Mater. 2022, 34, 2410–2421

rotation of the $PnCh_4^{3-}$ tetrahedra can be seen when observing the structure along the crystallographic [001] direction.[36] In addition to these two typical polymorphs, recently, a third polymorph was reported: at relatively high temperatures, around 520 °C, cubic Na_3PS_4 transforms into an orthorhombic structure (space group *Fddd*) possessing plastic crystal-like properties.[37]

Considering the diffusion pathways, theoretical work suggests that sodium ion migration happens by direct jumps between the stable sodium positions.[38,39] In the case of the cubic polymorph, this corresponds to jumps between 6*b* positions. In the case of the tetragonal polymorph, two different jumps can be identified, one from 2*b* to 4*d* corresponding to diffusion in the *a*-*b* plane and one between two neighboring 4*d* positions, corresponding to migration along the *c* axis. As suggested by theory, ^{23}Na nuclear magnetic resonance experiments and pair distribution function analyses, no substantial difference in activation barriers between the cubic and tetragonal polymorphs is expected for Na_3PnCh_4 due to the very similar Na^+ substructures and average structures.[33,38−40]

All four substitution series, $Na_3P_{1-x}Sb_xS_4$, $Na_3P_{1-x}Sb_xSe_4$, $Na_3PS_{4-y}Se_y$, and $Na_3SbS_{4-y}Se_y$, were prepared by classic high-temperature solid-state ampoule synthesis, and obtained X-ray diffractograms of all synthesized compounds can be found in the Supporting Information, Figures S1−S4. In the anionic substitution series, a phase transformation from tetragonal to cubic symmetry can be observed when S is substituted by Se. In the case of the $Na_3PS_{4-y}Se_y$, this phase transformation occurs between y = 1 and 1.5.[19] In the Sb analogues, the phase transition occurs at a lower Se content, namely, between y = 0.5 and 1 (compare Figure 2b), which is in accordance with the observations of Xiong and co-workers.[30] In the cationic substitution series, no phase transformation is observed, and for all compounds of the $Na_3P_{1-x}Sb_xS_4$ series, the tetragonal phase is present, while all Se analogues crystallize in the cubic polymorph at room temperature. For some compounds, reflections stemming from minor impurity phases could be observed (all below 3 wt %). The respective side phases are listed in the Supporting Information, Tables S1−S24.

Rietveld refinements were performed for all synthesized compounds to assess lattice parameters, $PnCh_4^{3-}$ tetrahedral (*Pn* = P, Sb; *Ch* = S, Se) and $NaCh_8$ dodecahedral volumes to better understand crystal structure changes upon substitution. All refinements and the extracted structural parameters are shown and tabulated in the Supporting Information in Figures S5−S8 and Tables S1−S24.

3.1.1. Unit Cell Volume Expansion. As seen in Figure 3a and Figure 3b, the overall unit cell volume increases linearly upon the introduction of Sb and Se, respectively, confirming that solid solutions are formed. Comparing Figure 3a,b, the overall larger expansion of the unit cell volume during anionic substitution is apparent. However, a direct comparison between the cationic and anionic substitution is complicated by a stoichiometric ratio of 1:4 between cations and anions and the different ionic radius differences for cations (Δr_{P-Sb} = 0.325(2) Å) and anions (Δr_{S-Se} = 0.14 Å).[41] Taking into account the cation to anion ratio of 1:4 and the respective ionic radii, one can define an average ionic radius R_{mean} of the $PnCh_4^{3-}$ tetrahedra[28]

$$R_{mean} = \left(\frac{r_P \cdot n_P + r_{Sb} \cdot n_{Sb} + r_S \cdot n_S + r_{Se} \cdot n_{Se}}{5} \right) \quad (1)$$

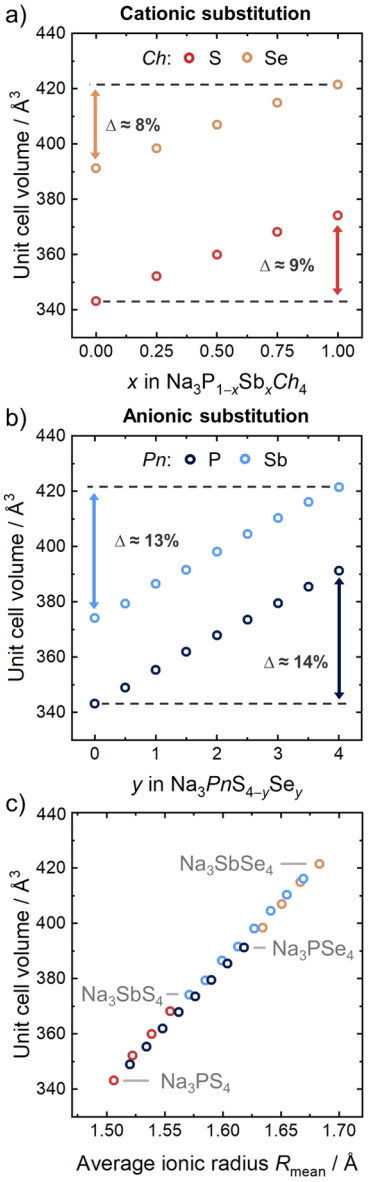

Figure 3. Evolution of the unit cell volume upon (a) cationic and (b) anionic substitution. The introduction of Sb and Se leads to an expansion of the unit cell due to the larger ionic radius. A more pronounced lattice expansion is found during anionic substitution. (c) Unit cell volume plotted against R_{mean}, the averaged ionic radius of the ions that constitute the $PnCh_4^{3-}$ tetrahedra, calculated from eq 1.

Here, r is the Shannon ionic radius[41] of P, Sb, S, and Se and n is the stoichiometric number of atoms per formula unit. For clarity, $n_{Sb} = 1 - n_P$ and $n_{Se} = 1 - n_S$. No ionic radius is tabulated for Sb in tetrahedral coordination with a charge state of +5. Therefore, the Sb radius was calculated from the known ionic radius of S^{2-} (1.84 Å)[41] and the Rietveld refinement determined the Sb−S bond length (2.335(2) Å) in Na_3SbS_4 to be r_{Sb} = 0.495(2). R_{mean} is found to correlate linearly with the unit cell volume, as seen in Figure 3c, showing that, under consideration of the stoichiometric ratio, the overall unit cell volume expansion can be approximately described on the basis of the different ionic radii.

3.1.2. $PnCh_4^{3-}$ Volume Expansion. The here determined $PnCh_4^{3-}$ volumes correspond to the volume bound by four *Ch* ions that surround the central *Pn* ion. The corners of this

https://doi.org/10.1021/acs.chemmater.1c04445
Chem. Mater. 2022, 34, 2410−2421

tetrahedron are defined by the crystallographic centers of the *Ch* ions. As shown in Figure 4a, for the cationic substitution series and in Figure 4b for the anionic substitution series, the tetrahedral volume increases upon the introduction of Sb and Se. In contrast to the unit cell volume, the tetrahedral volume expands more during cationic substitution. These stronger changes may be related to the larger relative ionic radius difference of the cations (Δr_{P-Sb} = 0.325(2) Å) compared to that of the anions (Δr_{S-Se} = 0.14 Å).[41] To investigate the tetrahedral size changes in the context of altered ionic radii in more detail, *Pn*−*Ch* bond lengths $d(Pn-Ch)_c$ can be calculated[28]

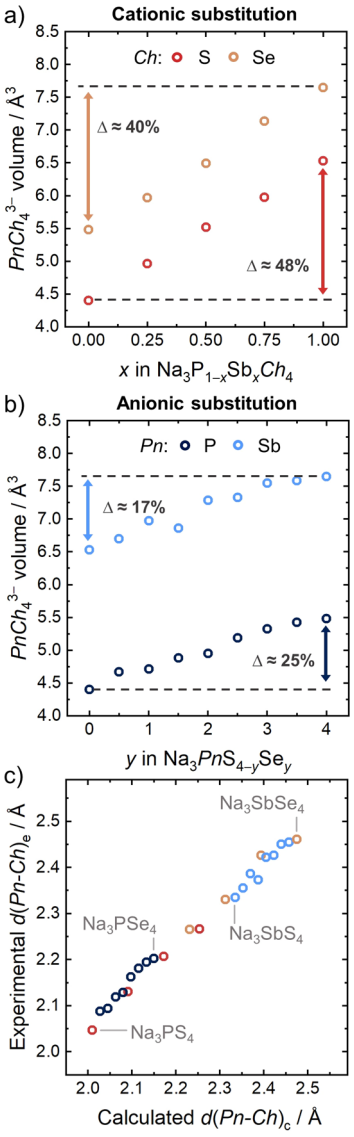

Figure 4. Evolution of the $PnCh_4^{3-}$ tetrahedral volume upon (a) cationic and (b) anionic substitution. The $PnCh_4^{3-}$ volume expands upon the introduction of Sb and Se due to the larger ionic radii. This expansion is more pronounced during the cationic than the anionic substitution. (c) Experimentally determined *Pn*−*Ch* bond length plotted against the calculated bond length using eq 2. The linear correlation between experimental and calculated values suggests that the *Pn*−*Ch* bond length can be described on the basis of a hard sphere model.

$$d(Pn-Ch)_c = (r_P n_P + r_{Sb} n_{Sb})_{Pn} + \left(\frac{r_S n_S + r_{Se} n_{Se}}{4}\right)_{Ch} \quad (2)$$

As seen in Figure 4c, a linear relationship was found between the average *Pn*−*Ch* bond distance determined from the Rietveld refinements and the bond distance calculated using eq 2. This suggests that the determined *Pn*−*Ch* bond length (a crystallographic average) can be well described and predicted by a hard sphere model in which the bond length is the sum of the individual ionic radii.[28] Additionally, bond lengths were calculated using a bond valence sum (BVS) approach, as provided in the Supporting Information. The hereby calculated bond lengths are in good agreement with the experimentally determined bond lengths.

While R_{mean} correlated linearly with the unit cell volume, different $PnCh_4^{3-}$ volumes were found for one single R_{mean} value (compare Figure S10a), highlighting the insufficiency of this metric for a description of $PnCh_4^{3-}$ size changes.[28] Vice versa, the calculated *Pn*−*Ch* bond lengths—using either a BVS approach or Shannon ionic radii—were found to be an insufficient descriptor for the unit cell volume changes, as shown in Figures S9b and S10b.

3.1.3. Na-Ch Polyhedral Expansion. In the tetragonal polymorph, two different Na−*Ch* coordination polyhedra can be defined for Na^+ occupying the Wyckoff 2*a* and the Wyckoff 4*d* position. In the cubic structure, only one coordination polyhedron type forms around the Wyckoff 6*a* position. For easier comparison of cubic and tetragonal phases, only similar coordination polyhedra, namely, $NaCh_8$ dodecahedra, were considered. Volumes of coordination polyhedra around the Wyckoff 4*d* position ($NaCh_6$ polyhedra) in the tetragonal phases are shown in the Supporting Information, Table S25. As seen in Figure 5a and Figure 5b, the $NaCh_8$ dodecahedra expand upon the introduction of Sb and Se, respectively. Like the unit cell volume, the volume of the $NaCh_8$ dodecahedra expands more during the anionic substitution than during the cationic substitution, which is not surprising, considering that the *Pn* ion is not directly participating in the bonds that constitute the $NaCh_8$ dodecahedron.

During cationic as well as during anionic substitution, the $NaCh_8$ volume expansion is caused by repulsive interactions between neighboring *Ch*. The replacement of S with Se, which has a larger electron shell, causes the expansion upon anionic substitution. During cationic substitution on the other hand, the $NaCh_8$ volume expansion is presumably caused indirectly by the expansion of the $PnCh_4^{3-}$ units. When the central ion of the tetrahedron is replaced by a larger one, the *Ch* ions on the corner of the tetrahedron are pushed away from the center, as shown in Figure 5c, which leads to a change of their relative position within the unit cell. Such a displacement of relative positions is connected to a change of polyhedral distortions. The angle β (see Figure 5c) can be used to identify distortion changes of the $NaCh_8$ polyhedra. As seen in Figure 5d, this angle changes drastically during cationic substitution and only moderately during anionic substitution. The changing distortion associated with larger β during cationic substitution indicates that the $NaCh_8$ volume expansion is driven by *Ch* ions being displaced against each other so that the increasing repulsive forces can only be accommodated by a volume expansion.

For the Na*Ch* and *PnCh* coordination polyhedra as well as for the unit cell, a volume increase upon cationic and anionic substitution was observed. The relative expansion of these

https://doi.org/10.1021/acs.chemmater.1c04445
Chem. Mater. 2022, 34, 2410−2421

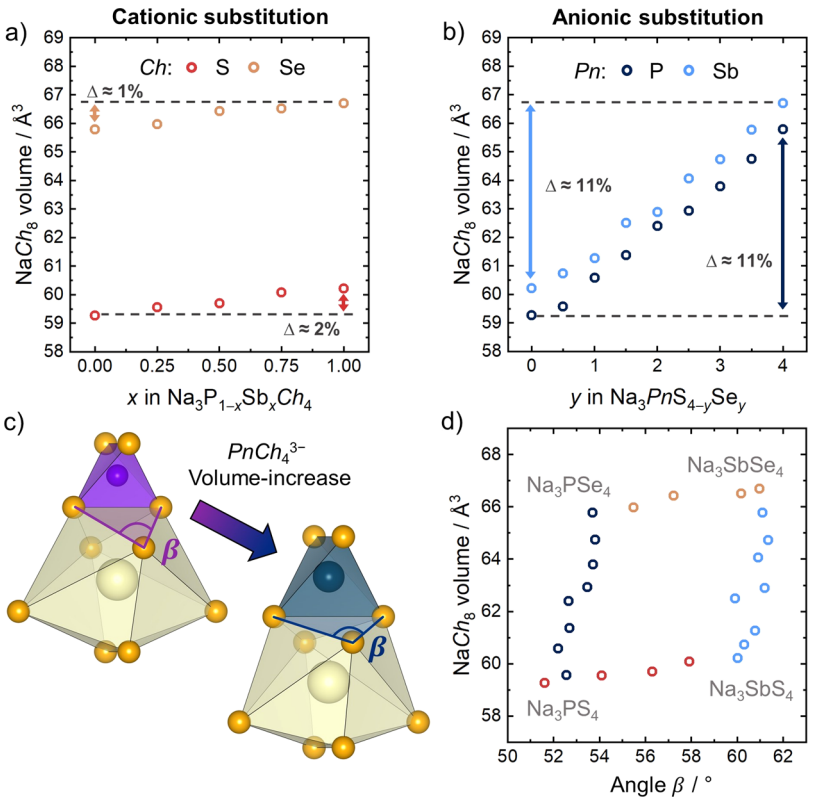

Figure 5. Volume changes of the $NaCh_8$ dodecahedra upon (a) cationic and (b) anionic substitution. The $NaCh_8$ volume expands upon the introduction of Sb and Se. This expansion is more pronounced during anionic than the cationic substitution. (c) Connectivity of the $NaCh_8$ and $PnCh_4^{3-}$ tetrahedra. The angle β can be used to investigate changes of the polyhedral distortion. During cationic substitution, the relative position of *Ch* ions changes, which leads to a change of β and with it the $NaCh_8$ polyhedral distortion. (d) $NaCh_8$ volume shown as a function of the angle β. The angle changes drastically during cationic substitution and only moderately during anionic substitution. The volume expansion during cationic substitution supposedly happens because the $NaCh_8$ volume has to accommodate for the increasing distortion.

volumes however was different for cationic and anionic substitution. Also, within one substitution series, the relative size changes of coordination polyhedra and the unit cell were differently pronounced, as summarized in Figure S11. In a simple substitution series, the distinction of relative size changes is easily overlooked. 2D substitution approaches on the other hand directly highlight these differences and are therefore an excellent method of gaining a deeper understanding of structural changes caused by compositional change. Specifically, the comparison of the four substitution series helps to understand that the volume increase upon the introduction of larger ions is more complex than just a uniform increase in all coordination polyhedra and the unit cell volume, which implies that the size changes of coordination polyhedra cannot be directly deduced from the size changes of the unit cell. This is especially relevant for the discussion of diffusion channel/diffusion bottleneck sizes, where often an increasing channel size is predicted from a growing unit cell, which may lead to wrong assumptions about the actual changes of the channel size. Thus, the diffusion bottleneck was investigated in detail.

3.1.4. Structural Changes of the Diffusion Bottleneck. The size of the diffusion bottleneck is expected to impose a crucial structural influence on the transport properties of a solid ionic conductor.[7,10,12] During the migration process, the ions that build the bottleneck need to move from their equilibrium position to create a free path for the migrating ion. This displacement of the host−lattice ions comes at an energetic cost, and a wide bottleneck should require less displacement and hence less energy for the diffusion process. Usually, the diffusion bottleneck corresponds to the contact area of two neighboring coordination polyhedra of the mobile ion. In the Na_3PnCh_4 structure, this contact area is defined by four *Ch* ions, which are highlighted in Figure 6a. The resulting bottleneck can be regarded as a distorted Ch_4 tetrahedron or a distorted square.[20] The Ch_4 tetrahedron turned out as an impractical metric for the diffusion bottleneck size in the whole substitution series due to the susceptibility of the tetrahedral volume to distortion changes, as further explained in the Supporting Information.

When describing the bottleneck as a distorted square, in which the corners are defined by the crystallographic positions of the *Ch* ions, the size of this square can be assessed from its diagonals. These correspond to the distance between two diagonally opposing *Ch* ion centers, i.e., a *Ch*−*Ch* distance, as shown in Figure 6a. In the cubic polymorph, both *Ch*−*Ch* distances within one square are the same. In the tetragonal polymorph on the other hand, the square is more distorted so that, for one square, two different *Ch*−*Ch* distances are found. Also, different *Ch*−*Ch* distances are found for the bottlenecks in the *a*-*b* plane and in the *c* direction. Consequently, four different *Ch*−*Ch* distances are present in the tetragonal polymorph, which are shown in Figure S14a−c. For a better comparison to the cubic structure, where only one *Ch*−*Ch* distance is found, an average *Ch*−*Ch* distance was calculated out of the four different *Ch*−*Ch* distances for all tetragonal polymorphs. Unaveraged *Ch*−*Ch* distances are shown in Figure S14d−f. Upon the introduction of Sb and Se, the

https://doi.org/10.1021/acs.chemmater.1c04445
Chem. Mater. 2022, 34, 2410−2421

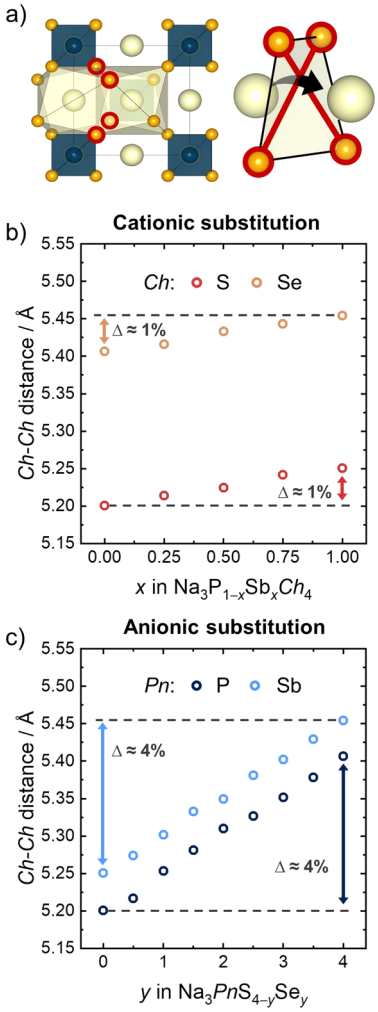

Figure 6. (a) Diffusion bottleneck in the Na_3PnCh_4 structure. The diffusion bottleneck consists of four *Ch* ions marked in red, which form a distorted square. The size of this square can be assessed from the square diagonals marked by red lines, which correspond to a crystallographic *Ch*−*Ch* distance. For the comparison of *Ch*−*Ch* distances in the cubic and tetragonal polymorph, an average over the four different *Ch*−*Ch* distances present in the tetragonal structure was calculated. The determined (averaged) *Ch*−*Ch* distances are shown in panel (b) for the cationic and panel (c) for the anionic substitution series. An increasing *Ch*−*Ch* distance is found upon the introduction of Sb and Se, with a more pronounced increase upon the anionic substitution.

(averaged) *Ch*−*Ch* distance was found to increase, as shown in Figure 6b and Figure 6c, respectively. This increase was more pronounced during the anionic than the cationic substitution, suggesting that the diffusion bottleneck is more widened upon anionic substitution. To study the influence of the changing diffusion bottleneck size on the activation barrier, temperature-dependent impedance spectroscopy measurements were carried out.

3.2. Transport Characterization. Temperature-dependent impedance spectroscopy was carried out to evaluate the ionic conductivities, activation barriers, and Arrhenius pre-factors. Figure 7a,b shows representative Nyquist plot impedance spectra of the ternary phases Na_3PS_4, Na_3SbS_4, Na_3PSe_4, and Na_3SbSe_4. The impedance data were fit with an equivalent circuit consisting of a parallel resistor/constant phase element (CPE) in series with a CPE to account for the

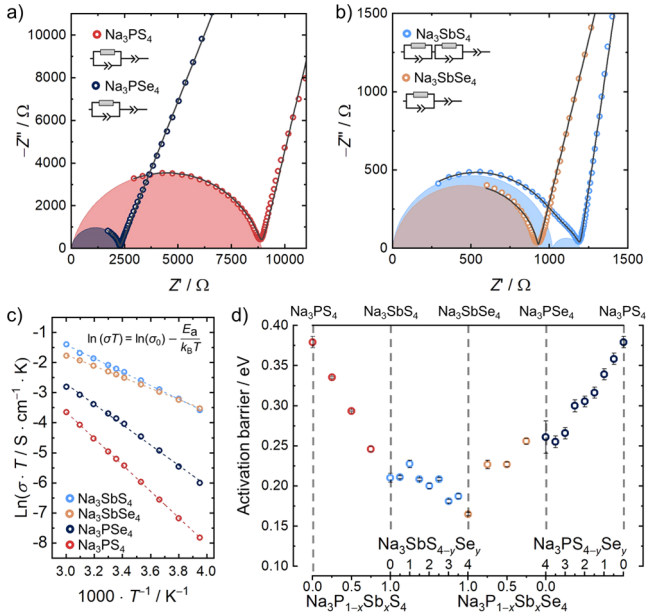

Figure 7. Representative Nyquist plots of (a) Na_3PS_4, Na_3PSe_4, (b) Na_3SbS_4, and Na_3SbSe_4 at 25 °C. The gray lines represent the obtained fit to the data, according to the depicted equivalent circuits. (c) Arrhenius plots of Na_3PS_4, Na_3SbS_4, Na_3PSe_4, and Na_3SbSe_4 between −20 and 60 °C. The Arrhenius equation is shown, with σ being the conductivity, σ_0 as the Arrhenius pre-factor, and E_a as the activation barrier. (d) Determined activation barriers for all four substitution series.

observed semicircle at high frequencies and the steep impedance increase at lower frequencies, which was attributed to the ion blocking electrodes. For the semicircle at high frequencies, ideality factors of ∼0.9 for most samples were determined. Quasi-capacitances calculated via the Brug equation[42] varied between substitution series and samples from 14 to 112 pF. With capacitances in the pF range and high ideality factors mainly between 0.8 and 0.9, the observed semicircle at high frequencies can be viewed as a predominantly in-grain conduction process.[43] All ideality factors, quasi-capacitances, relative density of pressed pellets, and representative impedance spectra of all samples are shown in the Supporting Information. For some impedance spectra, asymmetries of the semicircle and the linear spike at frequencies close to the *x* axis intercept were found, which were fitted with an additional R/CPE-element. The determined capacitances were in the nF range and higher, indicating processes connected to grain boundary conduction or surface roughness.[44,45] Ideality factors ranged from 0.8 down to 0.5. Presumably, different processes are present for low ideality factors; however, a deconvolution is not possible.

Figure 7c shows representative Arrhenius plots of Na_3PS_4, Na_3SbS_4, Na_3PSe_4, and Na_3SbSe_4. The activation barriers decrease upon the introduction of more polarizable ions, as shown in Figure 7d, which has been observed for many other materials as well.[8,19,23] However, due to the simultaneous decrease in the activation barrier and Arrhenius pre-factor, only a moderate increase in the ionic conductivity is found (see Figure S27a,b). The concurrent change of the activation barrier and pre-factor is described by the Meyer−Neldel rule and is observed in many solid ionic conductors.[46−49] Meyer−Neldel plots of all four substitution series are shown in Figure S28a, and determined Meyer−Neldel energies are shown in

https://doi.org/10.1021/acs.chemmater.1c04445
Chem. Mater. 2022, 34, 2410−2421

Figure S28b. Breaking of the Meyer−Neldel rule was observed in W-doped Na_3SbS_4 as an extremely fast ion conductor,[6] showing the potential for conductivity increase through aliovalent doping or substitution approaches.

Even though the investigated isoelectronic substitutions are only suitable for conductivity enhancements within the boundaries set by the Meyer−Neldel rule, the gathered data set is well suited to study the influence of the crystal structure on ionic transport. Specifically, the relevance of the diffusion channel size as a static descriptor for ionic transport was evaluated by investigating activation barrier changes with altered channel sizes and comparing between all four substitution series.

4. DISCUSSION

4.1. Influence of Bottleneck Size on the Activation Barrier. The diffusion bottleneck is expected to have a significant impact on the activation barrier height that intuitively should decrease with increasing bottleneck size.[7,14,50] Using the (averaged) *Ch*−*Ch* distance as the structural measure to describe the size of the diffusion bottleneck, we find a clear decrease in the activation barriers with increasing *Ch*−*Ch* distance for each individual substitution series (see Figure 8). However, there is not one unique relation that describes the whole substitution system. The slope (indicated by the dotted lines in Figure 8) is much steeper for the cationic substitution series, meaning that a widening of the diffusion bottleneck during cationic substitution is accompanied by a larger drop of the activation barrier compared to that arising from anionic substitution. If the changes of the activation barrier were mainly driven by the size of the diffusion bottleneck, then all of the slopes would be approximately equal but this is not observed. In other words, if the bottleneck had a dominant influence on the activation barrier, then the largest changes in the activation barrier should be found for the largest changes of the *Ch*−*Ch* distances, but the opposite is found. In addition, one *Ch*−*Ch* distance can clearly lead to two different activation barriers, and therefore, this bottleneck size is an insufficient descriptor for the activation barrier. Since the geometric descriptor alone fails to fully describe the activation barrier changes, possible influences of altered lattice dynamics on the activation barrier were investigated in more detail.

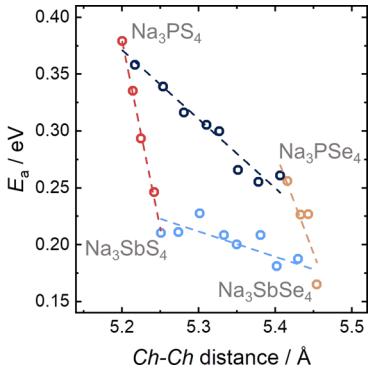

Figure 8. Activation barrier shown as a function of the crystallographic (averaged) *Ch*−*Ch* distance, used as a descriptor for the bottleneck size. For each single-substitution series, a clear decrease in the activation barrier with increasing bottleneck size is found. Considering the whole substitution series, however, differences between cationic and anionic substitution series are apparent. The activation barrier changes cannot be explained based on the diffusion bottleneck size changes.

4.2. Influence of Lattice Softness on the Activation Barrier. Recently, Debye frequencies determined from speed of sound measurements and average phonon frequencies were used to determine the lattice dynamics of ionic conductors.[15,19,33] While those descriptors have been shown to be excellent descriptors for the average lattice dynamics, they are only scarcely employed in solid electrolyte research since measurement equipment is often not available and calculation of phonon band centers is complex. Therefore, we propose the use of two other metrics, the melting temperature determined from differential scanning calorimetry (DSC) and the anharmonic weighted bulk modulus determined from temperature-dependent X-ray diffraction. Since these measurement techniques are already used in various solid-state chemistry groups, we hope that this will lower the entry barrier to study lattice dynamical changes in solids. In addition, melting temperatures and bulk moduli are not only attractive descriptors due to their accessibility. Since they are both macroscopic, thermodynamic quantities, they are well suited to capture changes of the average lattice dynamics and correlation of the melting temperatures and bulk moduli with the activation barriers have been reported for metals.[51] The here chosen descriptors were determined for Na_3PS_4, Na_3SbS_4, Na_3PSe_4, and Na_3SbSe_4.

The melting temperatures of materials are connected fundamentally to the forces acting between atoms, i.e., the bonding interactions. From a solid-state physics perspective, the bonding interactions/the bond strengths between atoms are described by force constants. For a harmonic oscillator, the force constant is inversely proportional to the square of the displacement, meaning that, in a rigid lattice with high force constants, the atoms are kept close to their equilibrium position, i.e., only small displacements occur. In soft lattices on the other hand, small force constants and large displacements are present, as schematically shown in Figure 9a. The Lindemann criterion relates the atomic displacement and thus the force constants to the melting temperature by stating that a solid melts once the displacement of an atom exceeds a certain threshold value, and the displaced atom starts interfering with a neighboring atom. In rigid lattices with large force constants, higher temperatures are necessary to reach this threshold displacement, compared to softer lattices, where lower temperatures are sufficient.[52]

The Lindemann criterion can be also expressed with the melting temperature as a function of the Debye temperature or corresponding Debye frequency, where the melting temperature is proportional to the square of the Debye temperature.[53] As mentioned above, the Debye temperature or the corresponding Debye frequency has been used repeatedly as an average descriptor for bond strengths in solids,[21,54,55] further highlighting the use of melting temperatures as a descriptor for average bonding interactions in a material. The melting temperatures are determined from DSC measurements shown in Figure S29. From the melting temperatures displayed in Figure 9b, we find that the lattice softens in the order Na_3PS_4 > Na_3PSe_4 > Na_3SbS_4 > Na_3SbSe_4, showing that the introduction of more polarizable and heavier ions leads to lattice softening effects. It also shows that the softening effect upon Sb substitution is more pronounced than upon Se substitution. In addition, the Debye frequency can be

https://doi.org/10.1021/acs.chemmater.1c04445
Chem. Mater. 2022, 34, 2410−2421

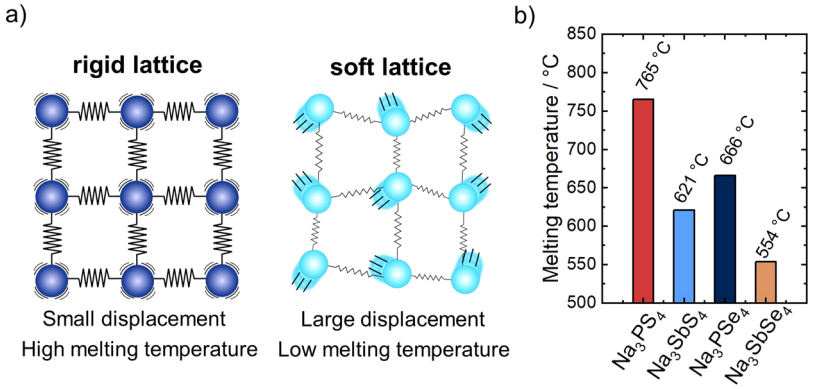

Figure 9. (a) Schematic overview of the relation between force constants/bond strength represented by springs, the thermally excited atom displacement and the corresponding melting temperature. (b) Melting temperatures of Na_3PS_4, Na_3SbS_4, Na_3PSe_4, and Na_3SbSe_4 as determined form DSC.

determined from speed of sound measurements and the melting temperature is a function of the Debye frequency according to the Lindemann criterion; a correlation between melting temperatures and speed of sound would be expected.

As a second descriptor for lattice softness, the bulk modulus B can be used, which is the inverse of the compressibility of the material and influenced by all present force constants in a crystal lattice.[56] It therefore is a suitable measure for the average bonding interactions in a solid. The bulk modulus not only can be determined from speed of sound measurements[57] but can be also extracted from lattice expansion as determined from temperature-dependent X-ray diffraction, which was the chosen method for this study. Using the Grüneisen parameter γ, the anharmonic bulk modulus B_γ can be defined by the heat capacity c_V and the thermal expansion coefficient α as[58]

$$B_\gamma = \frac{B}{\gamma} = \frac{c_V}{\alpha} \tag{3}$$

Since the heat capacity for $T > \theta_D$ (Debye temperature) converges to the Dulong–Petit limit, $c_V = 3k_B n$, where n is the number of atoms per volume and α can be extracted from temperature-dependent X-ray diffraction; then, B_γ is a modulus that can be obtained solely from diffraction measurements. θ_D of Na_3PS_4 can be calculated from the reported Debye frequency as being 199 K.[21] Since, for Na_3PS_4, $T > \theta_D$ is valid at room temperature, it will also be valid for the other three softer compounds, which justifies using the Dulong–Petit limit to calculate the anharmonic bulk modulus. Consequently, temperature-dependent X-ray diffraction was measured for Na_3PS_4, Na_3SbS_4, Na_3PSe_4, and Na_3SbSe_4 to assess their respective thermal expansion coefficients α at 300 K. All diffractograms, the retrieved crystallographic information, and the calculated α-values are provided in the Supporting Information. It should be mentioned that the calculated anharmonic bulk moduli and the melting temperatures inherently incorporate anharmonic properties of the investigated materials. For the anharmonic bulk modulus, this is directly seen from eq 3 since B_γ is not only a function of the bulk modulus but also the Grüneisen parameter. Melting itself can be described as the result of anharmonic events, during which ions are displaced so far from their equilibrium position that the solid configuration becomes instable. The role of anharmonicity for ionic transport processes has recently been discussed but is not yet fully understood.[59−61] As seen in Figure 10a, the determined anharmonic bulk moduli decrease together with the melting temperatures, confirming the lattice softening effect deduced from melting temperature changes. The validity of the observed lattice softening effect is corroborated by the fact that the two material properties were determined from different measurement approaches, one based on diffraction and the second one on calorimetric measurements.

Lattice softening is expected to result in lower activation barriers since with a weakening of the bonding interactions, i.e., smaller force constants, the overall vibrational potentials are flattened and less energy is necessary to displace the mobile ion toward a neighboring vacant lattice site.[8] In line with these expectations, the activation barriers decrease monotonically with the melting temperatures and the anharmonic bulk moduli, as shown Figure 10b and Figure 10c, respectively. For the geometric descriptor, i.e., the *Ch*−*Ch* distance, no such single relation for the activation barrier changes with the *Ch*−*Ch* distance was found, suggesting only a subordinate influence of bottleneck size on the activation barrier. The monotonous change of the activation barriers with the two dynamic descriptors on the other hand shows that lattice softening is the dominant factor for activation barrier changes in the Na_3PnCh_4 structure.

5. CONCLUSIONS

In this work, we presented a two-dimensional substitution approach for the system $Na_3P_{1-x}Sb_xS_{4-y}Se_y$ to gain a deeper understanding of crystal structure changes with composition and the impact that the altered crystal structure and bonding interactions have on the activation barrier for Na^+ conductivity.

Detailed structural characterizations revealed clear differences of polyhedral volume changes between the cationic and anionic substitution series and also between the different investigated coordination polyhedra, highlighting that the volume changes upon substitution are more complex than just a uniform expansion of all present polyhedra. In addition to the insights gathered on structural changes as a function of composition, the 2D approach helped to gain further insights on driving forces for activation barrier changes in the Na_3PnCh_4 structure. Investigation of the activation barrier and bottleneck size—represented by the *Ch*−*Ch* distance—showed that geometrical descriptors are not well suited to capture the activation barrier changes. Although structural descriptors, such as bottleneck sizes, have been used extensively to explain changes of the activation barrier, most

https://doi.org/10.1021/acs.chemmater.1c04445
Chem. Mater. 2022, 34, 2410−2421

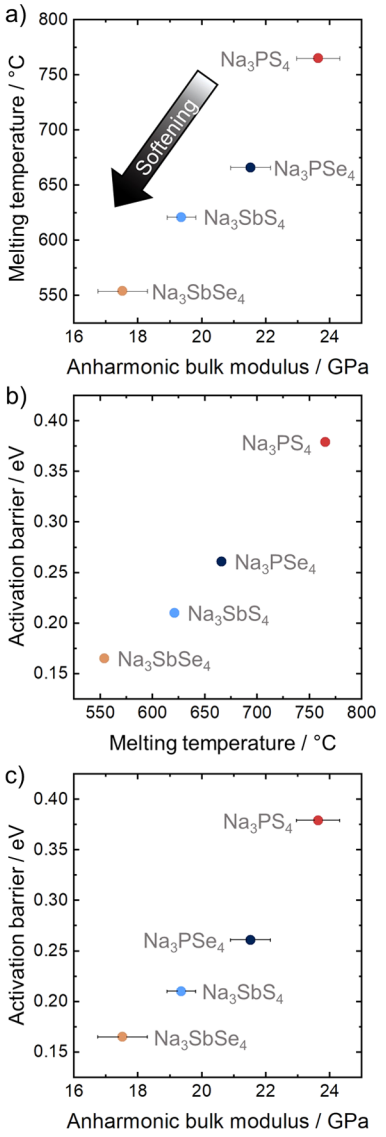

Figure 10. (a) Melting temperatures of the ternary, unsubstituted compounds, shown against the anharmonic bulk modulus B_γ as determined from temperature-dependent X-ray diffraction. Both quantities decrease simultaneously, validating the earlier observed lattice softening effect. (b) Activation barrier shown against the melting temperature and (c) the anharmonic bulk modulus B_γ. The decrease in the activation barrier with decreasing melting temperature and anharmonic bulk modulus corroborates, that the activation barrier changes observed for the different substitution series are mainly driven by the changes of the average bonding interactions, i.e., by lattice softening.

of these studies only make use of a single compositional substitution. Any single-substitution series of this study may also have led to the conclusion that the *Ch*−*Ch* distance is a suitable descriptor for the transport properties since a clear correlation between the bottleneck size and activation barrier is found for each individual substitution series. Only by using a two-dimensional substitution series, it is clear that static, geometric influences alone are insufficient to capture the changes in the activation barrier, making it necessary to also consider the influence of lattice dynamics. Lattice softening effects, i.e., weakening of bonding interactions, were studied on the basis of melting temperatures and the herein newly defined anharmonic bulk modulus B_γ. The activation barrier decreased monotonically with those dynamic descriptors, as opposed to what was found for the static descriptors. Hence, lattice softening was identified as the main driving force for the activation barrier changes.

It needs to be emphasized again that these findings would have hardly been made by the investigation of a single-substitution series since the convoluted structural and dynamical changes in isoelectronic substitution series deny the assignment of activation barrier changes to one or the other effect. The fact that the bottleneck size appeared to be a good descriptor for every single-substitution series but not for the whole structure family shows that the comparison of different substitution series helps to identify if a descriptor can be universally applied to a whole structure family. In contemporary discussions, structural parameters are often used to explain activation barrier changes, while lattice dynamical changes are often overlooked or treated as a minor effect. With the here presented work, we want to highlight the relevance of lattice softening effects for activation barriers, and the possibilities to uncover such effects by the use of two-dimensional substitution series also in other Na^+ and Li^+ solid electrolytes.

■ ASSOCIATED CONTENT

Supporting Information

The Supporting Information is available free of charge at https://pubs.acs.org/doi/10.1021/acs.chemmater.1c04445.

All X-ray diffractograms, Rietveld refinements, and corresponding structural parameters including temperature-dependent data of Na_3PS_4, Na_3SbS_4, Na_3PSe_4, and Na_3SbSe_4; $NaCh_6$ volumes as derived from Rietveld refinements; discussion of the Ch_4 bottleneck; *Ch*−*Ch* distances in tetragonal polymorphs; thermal expansion coefficients; Nyquist impedance spectra at 25 °C, associated capacitances, and ideality factors; Arrhenius plots; plots of ionic conductivities at 25 °C and Arrhenius pre-factors; Meyer−Neldel plot; and obtained DSC data (PDF)

All crystallographic information files (ZIP)

Temperature dependent structural data files (ZIP)

■ AUTHOR INFORMATION

Corresponding Author

Wolfgang G. Zeier − *Institute of Inorganic and Analytical Chemistry, University of Münster, Münster D-48149, Germany; Institut für Energie- und Klimaforschung (IEK), IEK-12: Helmholtz-Institut Münster, Forschungszentrum Jülich, Münster 48149, Germany;* orcid.org/0000-0001-7749-5089; Email: wzeier@uni-muenster.de

Authors

Paul Till − *Institute of Inorganic and Analytical Chemistry, University of Münster, Münster D-48149, Germany*

Matthias T. Agne − *Institut für Energie- und Klimaforschung (IEK), IEK-12: Helmholtz-Institut Münster, Forschungszentrum Jülich, Münster 48149, Germany*

Marvin A. Kraft − *Institute of Inorganic and Analytical Chemistry, University of Münster, Münster D-48149, Germany*

Matthieu Courty − *Laboratoire de Réactivité et de Chimie des Solides, CNRS-UMR no. 7314, Université de Picardie Jules Verne, Amiens F-80039, France*

https://doi.org/10.1021/acs.chemmater.1c04445
Chem. Mater. 2022, 34, 2410−2421

Theodosios Famprikis − *Laboratoire de Réactivité et de Chimie des Solides, CNRS-UMR no. 7314, Université de Picardie Jules Verne, Amiens F-80039, France; Department of Radiation Science and Technology, Delft University of Technology, Delft 2629 JB, Netherlands;* orcid.org/0000-0002-7946-1445

Michael Ghidiu − *Institute of Physical Chemistry, Justus-Liebig-University Giessen, Giessen D-35392, Germany*

Thorben Krauskopf − *Institute of Physical Chemistry, Justus-Liebig-University Giessen, Giessen D-35392, Germany*

Christian Masquelier − *Laboratoire de Réactivité et de Chimie des Solides, CNRS-UMR no. 7314, Université de Picardie Jules Verne, Amiens F-80039, France;* orcid.org/0000-0001-7289-1015

Complete contact information is available at: https://pubs.acs.org/10.1021/acs.chemmater.1c04445

Notes

The authors declare no competing financial interest.

■ ACKNOWLEDGMENTS

The research was supported by the Federal Ministry of Education and Research (BMBF) within the project NASEBER under grant number 03XP0187C. This work was carried out with the support of Diamond Light Source, instrument I11 (reference no. CY24332). The authors would also like to thank the Beamline Scientists Dr. Claire Murray and Dr. Stephen Thompson for assistance during experiment preparation and data collection.

■ REFERENCES

(1) Janek, J.; Zeier, W. G. A Solid Future for Battery Development. *Nat. Energy* **2016**, *1*, 16141.

(2) Fan, L.; Wei, S.; Li, S.; Li, Q.; Lu, Y. Recent Progress of the Solid-State Electrolytes for High-Energy Metal-Based Batteries. *Adv. Energy Mater.* **2018**, *8*, 1−31.

(3) Kato, Y.; Hori, S.; Saito, T.; Suzuki, K.; Hirayama, M.; Mitsui, A.; Yonemura, M.; Iba, H.; Kanno, R. High-Power All-Solid-State Batteries Using Sulfide Superionic Conductors. *Nat. Energy* **2016**, *1*, 1−7.

(4) Sun, Y.; Suzuki, K.; Hori, S.; Hirayama, M.; Kanno, R. Superionic Conductors: $Li_{10+\delta}[Sn_ySi_{1-y}]_{1+\delta}P_{2-\delta}S_{12}$ with a $Li_{10}GeP_2S_{12}$-Type Structure in the Li_3PS_4-Li_4SnS_4-Li_4SiS_4 Quasi-Ternary System. *Chem. Mater.* **2017**, *29*, 5858−5864.

(5) Adeli, P.; Bazak, J. D.; Park, K. H.; Kochetkov, I.; Huq, A.; Goward, G. R.; Nazar, L. F. Boosting Solid-State Diffusivity and Conductivity in Lithium Superionic Argyrodites by Halide Substitution. *Angew. Chem., Int. Ed.* **2019**, *58*, 8681−8686.

(6) Fuchs, T.; Culver, S. P.; Till, P.; Zeier, W. G. Defect-Mediated Conductivity Enhancements in $Na_{3-x}Pn_{1-x}W_xS_4$ (*Pn* = P, Sb) Using Aliovalent Substitutions. *ACS Energy Lett.* **2019**, *5*, 146−151.

(7) Ohno, S.; Banik, A.; Dewald, G. F.; Kraft, M. A.; Krauskopf, T.; Minafra, N.; Till, P.; Weiss, M.; Zeier, W. G. Materials Design of Ionic Conductors for Solid State Batteries. *Prog. Energy* **2020**, *2*, No. 022001.

(8) Muy, S.; Bachman, J. C.; Giordano, L.; Chang, H. H.; Abernathy, D. L.; Bansal, D.; Delaire, O.; Hori, S.; Kanno, R.; Maglia, F.; Lupart, S.; Lamp, P.; Shao-Horn, Y. Tuning Mobility and Stability of Lithium Ion Conductors Based on Lattice Dynamics. *Energy Environ. Sci.* **2018**, *11*, 850−859.

(9) Bachman, J. C.; Muy, S.; Grimaud, A.; Chang, H.-H.; Pour, N.; Lux, S. F.; Paschos, O.; Maglia, F.; Lupart, S.; Lamp, P.; Giordano, L.; Shao-Horn, Y. Inorganic Solid-State Electrolytes for Lithium Batteries: Mechanisms and Properties Governing Ion Conduction. *Chem. Rev.* **2016**, *116*, 140−162.

(10) Culver, S. P.; Koerver, R.; Krauskopf, T.; Zeier, W. G. Designing Ionic Conductors: The Interplay between Structural Phenomena and Interfaces in Thiophosphate-Based Solid-State Batteries. *Chem. Mater.* **2018**, *30*, 4179−4192.

(11) Lin, Y. Y.; Yong, A. X. B.; Gustafson, W. J.; Reedy, C. N.; Ertekin, E.; Krogstad, J. A.; Perry, N. H. Toward Design of Cation Transport in Solid-State Battery Electrolytes: Structure-Dynamics Relationships. *Curr. Opin. Solid State Mater. Sci.* **2020**, *24*, 100875.

(12) Wang, Y.; Richards, W. D.; Ong, S. P.; Miara, L. J.; Kim, J. C.; Mo, Y.; Ceder, G. Design Principles for Solid-State Lithium Superionic Conductors. *Nat. Mater.* **2015**, *14*, 1026−1031.

(13) Xu, Z.; Chen, X.; Chen, R.; Li, X.; Zhu, H. Anion Charge and Lattice Volume Dependent Lithium Ion Migration in Compounds with Fcc Anion Sublattices. *npj Comput. Mater.* **2020**, *6*, 1−8.

(14) Martínez-Juárez, A.; Pecharromán, C.; Iglesias, J. E.; Rojo, J. M. Relationship between Activation Energy and Bottleneck Size for Li^+ Ion Conduction in NASICON Materials of Composition $LiMM'(PO_4)_3$; *M*, *M*′ = Ge, Ti, Sn, Hf. *J. Phys. Chem. B* **1998**, *102*, 372−375.

(15) Muy, S.; Schlem, R.; Shao-Horn, Y.; Zeier, W. G. Phonon−Ion Interactions: Designing Ion Mobility Based on Lattice Dynamics. *Adv. Energy Mater.* **2021**, 2002787.

(16) George, H.; Vineyard. Frequency Factors and Isotope Effects in Solid State Rate Processes. *J. Phys. Chem. Solids* **1957**, *3*, 121−127.

(17) Allen, S. J.; Remeika, J. P. Direct Measurement of the Attempt Frequency for Ion Diffusion in Ag and Na β-Alumina. *Phys. Rev. Lett.* **1974**, *33*, 1478−1481.

(18) Wakamura, K. Roles of Phonon Amplitude and Low-Energy Optical Phonons on Superionic Conduction. *Phys. Rev. B* **1997**, *56*, 11593−11599.

(19) Kraft, M. A.; Culver, S. P.; Calderon, M.; Böcher, F.; Krauskopf, T.; Senyshyn, A.; Dietrich, C.; Zevalkink, A.; Janek, J.; Zeier, W. G. Influence of Lattice Polarizability on the Ionic Conductivity in the Lithium Superionic Argyrodites Li_6PS_5X (*X* = Cl, Br, I). *J. Am. Chem. Soc.* **2017**, *139*, 10909−10918.

(20) Krauskopf, T.; Pompe, C.; Kraft, M. A.; Zeier, W. G. Influence of Lattice Dynamics on Na^+ Transport in the Solid Electrolyte $Na_3PS_{4-x}Se_x$. *Chem. Mater.* **2017**, *29*, 8859−8869.

(21) Krauskopf, T.; Muy, S.; Culver, S. P.; Ohno, S.; Delaire, O.; Shao-Horn, Y.; Zeier, W. G. Comparing the Descriptors for Investigating the Influence of Lattice Dynamics on Ionic Transport Using the Superionic Conductor $Na_3PS_{4-x}Se_x$. *J. Am. Chem. Soc.* **2018**, *140*, 14464−14473.

(22) Haas, C. W. On the Necessity for Invoking a Free-Ion-like Model for the Super Ionic Conductors. *J. Solid State Chem.* **1973**, *7*, 155−157.

(23) Kanno, R.; Murayama, M. Lithium Ionic Conductor Thio-LISICON: The Li_2S-GeS_2-P_2S_5 System. *J. Electrochem. Soc.* **2001**, *148*, A742−A746.

(24) Reddy, M. V.; Julien, C. M.; Mauger, A.; Zaghib, K. Sulfide and Oxide Inorganic Solid Electrolytes for All-Solid-State Li Batteries: A Review. *Nanomaterials* **2020**, *10*, 1−80.

(25) Culver, S. P.; Squires, A. G.; Minafra, N.; Armstrong, C. W. F.; Krauskopf, T.; Böcher, F.; Li, C.; Morgan, B. J.; Zeier, W. G. Evidence for a Solid-Electrolyte Inductive Effect in the Superionic Conductor $Li_{10}Ge_{1-x}Sn_xP_2S_{12}$. *J. Am. Chem. Soc.* **2020**, *142*, 21210−21219.

(26) Weiss, M.; Weber, D. A.; Senyshyn, A.; Janek, J.; Zeier, W. G. Correlating Transport and Structural Properties in $Li_{1+x}Al_xGe_{2-x}(PO_4)_3$ (LAGP) Prepared from Aqueous Solution. *ACS Appl. Mater. Interfaces* **2018**, *10*, 10935−10944.

(27) Duchardt, M.; Neuberger, S.; Ruschewitz, U.; Krauskopf, T.; Zeier, W. G.; Schmedt auf Der Günne, J.; Adams, S.; Roling, B.; Dehnen, S. Superion Conductor $Na_{11.1}Sn_{2.1}P_{0.9}Se_{12}$: Lowering the Activation Barrier of Na^+ Conduction in Quaternary 1-4-5-6 Electrolytes. *Chem. Mater.* **2018**, *30*, 4134−4139.

(28) Minafra, N.; Hogrefe, K.; Barbon, F.; Helm, B.; Li, C.; Wilkening, H. M. R.; Zeier, W. G. Two-Dimensional Substitution: Toward a Better Understanding of the Structure−Transport Correlations in the Li-Superionic Thio-LISICONs. *Chem. Mater.* **2021**, *33*, 727−740.

(29) Wang, H.; Chen, Y.; Hood, Z. D.; Sahu, G.; Pandian, A. S.; Keum, J. K.; An, K.; Liang, C. An Air-Stable Na_3SbS_4 Superionic Conductor Prepared by a Rapid and Economic Synthetic Procedure. *Angew. Chem., Int. Ed.* **2016**, *55*, 8551−8555.
(30) Xiong, S.; Liu, Z.; Rong, H.; Wang, H.; McDaniel, M.; Chen, H. $Na_3SbSe_{4-x}S_x$ as Sodium Superionic Conductors. *Sci. Rep.* **2018**, *8*, 9146.
(31) Wang, N.; Yang, K.; Zhang, L.; Yan, X.; Wang, L.; Xu, B. Improvement in Ion Transport in Na_3PSe_4−Na_3SbSe_4 by Sb Substitution. *J. Mater. Sci.* **2018**, *53*, 1987−1994.
(32) Hayashi, A.; Masuzawa, N.; Yubuchi, S.; Tsuji, F.; Hotehama, C.; Sakuda, A.; Tatsumisago, M. A Sodium-Ion Sulfide Solid Electrolyte with Unprecedented Conductivity at Room Temperature. *Nat. Commun.* **2019**, *10*, 5266.
(33) Krauskopf, T.; Culver, S. P.; Zeier, W. G. Local Tetragonal Structure of the Cubic Superionic Conductor Na_3PS_4. *Inorg. Chem.* **2018**, *57*, 4739−4744.
(34) Coelho, A. A. TOPAS and TOPAS-Academic: An Optimization Program Integrating Computer Algebra and Crystallographic Objects Written in C++: An. *J. Appl. Crystallogr.* **2018**, *51*, 210−218.
(35) Seidel, S.; Zeier, W. G.; Pöttgen, R. The Polymorphs of the Na^+ Ion Conductor Na_3PS_4 Viewed from the Perspective of a Group-Subgroup Scheme. *Z. Kristallogr. Cryst. Mater.* **2020**, *235*, 1−6.
(36) Famprikis, T.; Bouyanfif, H.; Canepa, P.; Zbiri, M.; Dawson, J. A.; Suard, E.; Fauth, F.; Playford, H. Y.; Dambournet, D.; Borkiewicz, O. J.; Courty, M.; Clemens, O.; Chotard, J. N.; Islam, M. S.; Masquelier, C.; Famprikis, T.; Islam, M. S. Insights into the Rich Polymorphism of the Na^+ Ion Conductor Na_3PS_4 from the Perspective of Variable-Temperature Diffraction and Spectroscopy. *Chem. Mater.* **2021**, *33*, 5652−5667.
(37) Famprikis, T.; Dawson, J. A.; Fauth, F.; Clemens, O.; Suard, E.; Fleutot, B.; Courty, M.; Chotard, J.-N.; Islam, M. S.; Masquelier, C. A New Superionic Plastic Polymorph of the Na^+ Conductor Na_3PS_4. *ACS Mater. Lett.* **2019**, *1*, 641−646.
(38) de Klerk, N. J. J.; Wagemaker, M. Diffusion Mechanism of the Sodium-Ion Solid Electrolyte Na_3PS_4 and Potential Improvements of Halogen Doping. *Chem. Mater.* **2016**, *28*, 3122−3130.
(39) Rush, L. E.; Hood, Z. D.; Holzwarth, N. A. W. Unraveling the Electrolyte Properties of Na_3SbS_4 through Computation and Experiment. *Phys. Rev. Mater.* **2017**, *1*, No. 075405.
(40) Yu, C.; Ganapathy, S.; De Klerk, N. J. J.; Van Eck, E. R. H.; Wagemaker, M. Na-Ion Dynamics in Tetragonal and Cubic Na_3PS_4, a Na-Ion Conductor for Solid State Na-Ion Batteries. *J. Mater. Chem. A* **2016**, *4*, 15095−15105.
(41) Shannon, R. D. Revised Effective Ionic Radii and Systematic Studies of Interatomic Distances in Halides and Chalcogenides. *Acta Crystallogr. Sect. A* **1976**, *32*, 751.
(42) Brug, G. J.; Van den Eeden, A. L. G.; Sluyters-Rehbach, M.; Sluyters, J. H. The Analysis of Electrode Impedances Complicated by the Presence of a Constant Phase Element. *J. Electroanal. Chem.* **1984**, *176*, 275−295.
(43) Irvine, J. T. S.; Sinclair, D. C.; West, A. R. Electroceramics: Characterization by Impedance Spectroscopy. *Adv. Mater.* **1990**, *2*, 132−138.
(44) David, I. N.; Thompson, T.; Wolfenstine, J.; Allen, J. L.; Sakamoto, J. Microstructure and Li-Ion Conductivity of Hot-Pressed Cubic $Li_7La_3Zr_2O_{12}$. *J. Am. Ceram. Soc.* **2015**, *98*, 1209−1214.
(45) Huggins, R. A. Simple Method to Determine Electronic Conductivity and Ionic Components of the Conductors in Mixed a Review. *Ionics* **2002**, *8*, 300−313.
(46) Yelon, A.; Movaghar, B. Microscopic Explanation of the Compensation (Meyer-Neldel) Rule. *Phys. Rev. Lett.* **1990**, *65*, 618−620.
(47) Yelon, A.; Movaghar, B.; Crandall, R. S. Multi-Excitation Entropy: Its Role in Thermodynamics and Kinetics. *Rep. Prog. Phys.* **2006**, *69*, 1145−1194.
(48) Gao, Y.; Li, N.; Wu, Y.; Yang, W.; Bo, S. H. Rethinking the Design of Ionic Conductors Using Meyer−Neldel−Conductivity Plot. *Adv. Energy Mater.* **2021**, *11*, 2100325.
(49) Muy, S.; Bachman, J. C.; Chang, H. H.; Giordano, L.; Maglia, F.; Lupart, S.; Lamp, P.; Zeier, W. G.; Shao-Horn, Y. Lithium Conductivity and Meyer-Neldel Rule in Li_3PO_4 -Li_3VO_4 - Li_4GeO_4 Lithium Superionic Conductors. *Chem. Mater.* **2018**, *30*, 5573−5582.
(50) Chen, F.; Xu, L.; Li, J.; Yang, Y.; Shen, Q. Effect of Bottleneck Size on Lithium Migration in Lithium Garnets $Li_7La_3Zr_2O_{12}$ (LLZO). *Ionics* **2020**, *26*, 3193−3198.
(51) Tiwari, G.P.; Mehtrota, R.S. ;Iijima, Y. In *Diffusion Processes in Advanced Technological Materials*; Gupta, D., Eds; William Andrew, Inc.: Norwich, 2005; Chapter 2, pp. 69−111.
(52) Grimvall, G.; Sjödin, S. Correlation of Properties of Materials to Debye and Melting Temperatures. *Phys. Scr.* **1974**, *10*, 340−352.
(53) Rabinovich, S.; Voronel, A.; Peretzman, L. Generalisation of the Lindemann Criterion for Disordered Mixed Crystals. *J. Phys. C Solid State Phys.* **1988**, *21*, 5943−5952.
(54) Hanus, R.; Agne, M. T.; Rettie, A. J. E.; Chen, Z.; Tan, G.; Chung, D. Y.; Kanatzidis, M. G.; Pei, Y.; Voorhees, P. W.; Snyder, G. J. Lattice Softening Significantly Reduces Thermal Conductivity and Leads to High Thermoelectric Efficiency. *Adv. Mater.* **2019**, *31*, 1900108.
(55) Schlem, R.; Ghidiu, M.; Culver, S. P.; Hansen, A. L.; Zeier, W. G. Changing the Static and Dynamic Lattice Effects for the Improvement of the Ionic Transport Properties within the Argyrodite $Li_6PS_{5-x}Se_xI$. *ACS Appl. Energy Mater.* **2020**, *3*, 9−18.
(56) Kittel, C. *Introduction to Solid State Physics;* John Wiley and Sons, Inc.: Hoboken, 2005.
(57) Anderson, O. L. A Simplified Method for Calculating the Debye Temperature from Elastic Constants. *J. Phys. Chem. Solids* **1963**, *24*, 909−917.
(58) Wallace, D. C. *Thermodynamics of Crystals*; Dover: New York, 1998.
(59) Brenner, T. M.; Gehrmann, C.; Korobko, R.; Livneh, T.; Egger, D. A.; Yaffe, O. Anharmonic Host-Lattice Dynamics Enable Fast Ion Conduction in Superionic AgI. *Phys. Rev. Mater.* **2020**, *4*, 115402.
(60) Ding, J.; Niedziela, J. L.; Bansal, D.; Wang, J.; He, X.; May, A. F.; Ehlers, G.; Abernathy, D. L.; Said, A.; Alatas, A.; Ren, Y.; Arya, G.; Delaire, O. Anharmonic Lattice Dynamics and Superionic Transition in $AgCrSe_2$. *Proc. Natl. Acad. Sci. U. S. A.* **2020**, *117*, 3930−3937.
(61) Niedziela, J. L.; Bansal, D.; May, A. F.; Ding, J.; Lanigan-Atkins, T.; Ehlers, G.; Abernathy, D. L.; Said, A.; Delaire, O. Selective Breakdown of Phonon Quasiparticles across Superionic Transition in $CuCrSe_2$. *Nat. Phys.* **2019**, *15*, 73−78.

NOTE ADDED AFTER ASAP PUBLICATION

This paper was published ASAP on February 25, 2022, with an error in the title of the paper and Supporting Information file. The corrected versions were reposted on February 25, 2022.

https://doi.org/10.1021/acs.chemmater.1c04445
Chem. Mater. 2022, 34, 2410−2421